



Development of an oxygen-evolution electrode from 316L stainless steel: Application to the oxygen evolution reaction in aqueous lithium–air batteries

Florian Moureaux ^{a,b}, Philippe Stevens ^a, Gwenaëlle Toussaint ^a, Marian Chatenet ^{b,*}

^a *Électricité de France, R&D, Laboratoire des matériaux électriques, LME, Groupe des batteries et gestionnaires d'énergie, M29, Avenue des Renardières, 77818 Moret sur Loing, France*

^b *Laboratoire d'Electrochimie et de Physicochimie des Matériaux et des Interfaces, LEPMI, UMR 5279 CNRS/Grenoble-INP/Université de Savoie/Université Joseph Fourier, 1130 rue de la piscine, BP75, 38402 Saint Martin d'Hères Cedex, France*

HIGHLIGHTS

- 316L stainless steel is a stable and competitive oxygen-evolution electrode in LiOH.
- A catalytic film spontaneously forms during operation, heightening the electrode performance.
- 3000 h of operation in oxygen evolution in LiOH electrolyte were reached experimentally.

ARTICLE INFO

Article history:

Received 28 September 2012

Received in revised form

13 November 2012

Accepted 29 November 2012

Available online 12 December 2012

Keywords:

Lithium–air batteries

Oxygen evolution reaction (OER)

Alkaline LiOH medium

Electrocatalyst

316L stainless steel

Nickel oxides

ABSTRACT

The use of commercial 316L stainless steel as a simple, stable and competitive oxygen-evolution electrode in alkaline media for aqueous lithium–air batteries has been studied. In addition to the electrochemical characterization, the electrode was analyzed by scanning electron microscopy (SEM), transmission electron microscopy (TEM), X-ray energy dispersive spectroscopy (X-EDS), X-ray photoelectron spectroscopy (XPS), X-ray diffraction (XRD), Raman spectroscopy and elemental analyses via inductively coupled plasma atomic emission spectroscopy (ICP-AES). The spontaneous formation of a catalytic film, during the aging test, gives rise to interesting electrode performances. Indeed, this film, containing a large part of nanocrystalline nickel oxides (83 at% of cationic composition), catalyzes the oxygen evolution reaction via two phenomena: an increase of the roughness of the electrode surface and a hypo–hyper d interbonding effect, due to the presence of well dispersed additives of Fe and Cr in the film.

© 2012 Elsevier B.V. All rights reserved.

1. Introduction

The success of the electric vehicles is highly dependent on the development of batteries presenting high energy densities, safe use and low-cost. Although lithium-ion batteries [1–6] have met a large commercial success for the powering of portable electronic devices, their limited energy density (<200 Wh kg^{−1}) and their high prices are both drawbacks for the electric vehicle market other than for niche applications. Very high energy densities are however possible in lithium–air batteries, because oxygen is not stored in the battery but is directly extracted from the ambient atmosphere, yielding a theoretical energy density of 13 kWh kg^{−1} (Li). This is

a theoretical value based on the weight of lithium metal, and a practical Li–air systems will probably not reach more than 600–1500 Wh kg^{−1} (because of kinetic limitations and system requirements, e.g. excess Li, mass of “inactive materials” and electrolyte) [7–10], but these latter values are still 3–8 times larger than for the present state-of-the-art lithium generators.

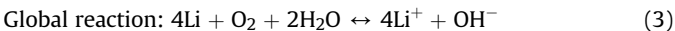
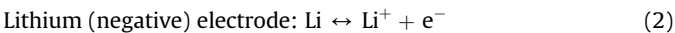
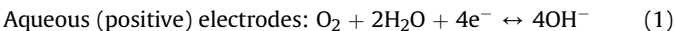
The first report of a rechargeable lithium–air cell originates from Abraham and Jiang in 1996 [11], soon followed by others [12–15]. In their configuration, the electrochemical reactions occur in organic electrolyte, to produce Li₂O₂ as a discharge product. This anhydrous lithium–air system is hindered by the insolubility of Li₂O₂, which generates major operational problems, like blocking of the pores in the air electrode, formation of a resistive layer and large charge voltages.

An alternative lithium–air concept, operating under aqueous electrolyte, has been patented by the PolyPlus Company in 2007

* Corresponding author. Tel.: +33 476 82 65 88; fax: +33 476 82 67 77.

E-mail address: Marian.Chatenet@grenoble-inp.fr (M. Chatenet).

[16–18]. In this system, the lithium metal is protected from the aqueous electrolyte by a lithium ion conducting glass film [19,20] and the product of the discharge reaction is stored in the aqueous electrolyte and not in the air electrode [9,21,22]. The electrode reactions of an aqueous Li-air battery correspond to Equations (1)–(3):



A standard air electrode for alkaline electrolyte can be used in this system, such as those developed for alkaline fuel cells or zinc-air batteries. However, this type of air electrode is designed to work as an oxygen reduction reaction (ORR) electrode only. It is composed of a catalyst supported onto carbon powder organized into a 3D porous structure. The catalyst and carbon materials are subjected to corrosion at high potential during charging process, which, coupled to the oxygen gas evolution, favors mechanical breakdown of this fragile porous structure and subsequent electrode/system failure. The use of a third electrode, dedicated to the oxygen evolution reaction (OER), is an interesting solution to avoid this problem [23–25] (Fig. 1). This third electrode is not necessarily a penalty for the energy density of the battery, because it can be designed to be lightweight and small in volume. Moreover, optimized and separate catalysts can also be used for both the OER and ORR, which would enhance the system stability and the energy efficiencies [7,24].

This study deals in particular with the development of an OER-dedicated electrode used to charge of the aqueous Li-air battery. In the aqueous lithium–air developed by EDF and its partners [9], this reaction occurs in saturated LiOH to produce oxygen. In order to reduce the costs, the chosen material should preferentially be selected from the d-block 4th period of the periodic table (Fe, Co, Ni, ...), because of the lower price and larger availability of these metals compared to other transition-metals. Many studies have in the past focused on such cobalt-oxide-catalyzed electrodes (Co_3O_4 and NiCo_2O_4). However the long term performance of these catalyst-coated electrodes, made by different fabrication processes (sol–gel or electrochemical deposition), were found to be unstable, had poor performances and lacked reproducibility in our tests conditions [26]. Simple 316L stainless steel, which was chosen as the substrate for the above-mentioned cobalt oxide catalyst

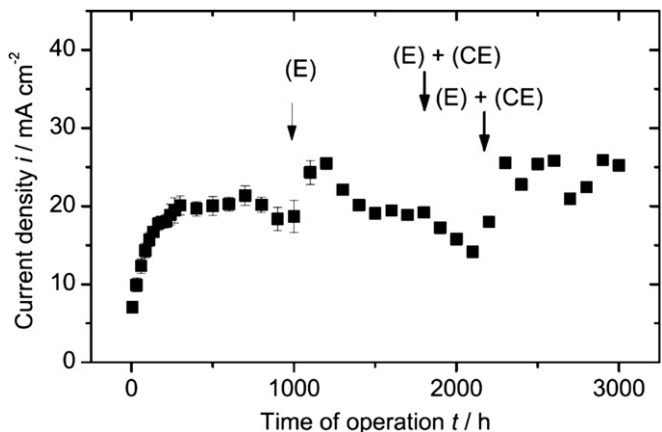


Fig. 2. Long-time polarization of the 316L stainless steel at 0.8 V vs. Hg/HgO – 1 M KOH; 5 M LiOH; $23 < T < 27$ °C; uncorrected for ohmic drop; statistical data obtained up to 1800 h; (E) and (CE) symbolize the replacement of the electrolyte and counter electrode, respectively.

deposits, is a cheaper alternative for the development of an OER electrode. This paper provides a characterization of such an OER electrode by combining physicochemical analyses (scanning electron microscopy (SEM), transmission electron microscopy (TEM), X-ray energy dispersive spectroscopy (X-EDS), X-ray photoelectron spectroscopy (XPS), X-ray diffraction (XRD), elemental analyses via inductively coupled plasma atomic emission spectroscopy (ICP-AES), Raman Spectroscopy) and electrochemical analyses prior/during/after a long-term operation (ca. 3000 h¹).

2. Experimental

The electrochemical characterization of the electrode was carried out in a three electrodes gas-tight cell (see Supplementary Figure S1). The carbonation of the electrolyte by CO_2 from air can therefore be neglected. The working electrode was a 316L stainless steel plate, provided by Goodfellow, with a geometrical surface area: $S_{\text{geo}} = 2 \text{ cm}^2$; the apparent current densities are referred to this value. The reference and the counter electrodes were Hg/HgO – 1 M KOH and a copper electrode ($S_{\text{geo}} \approx 4 \text{ cm}^2$), respectively. All potentials were expressed versus the Hg/HgO – 1 M KOH reference electrode and were corrected manually for the iR drop, itself being determined from the high frequency resistance values measured by electrochemical impedance spectroscopy. Before use, the electrodes were degreased with heptane/acetone and then dried in air. The electrochemical tests were carried out with a numerical VMP3 potentiostat–galvanostat from Bio-Logic[®].

The electrode stability tests were performed at a constant potential of 0.8 V vs. Hg–HgO/1 M KOH. The current was interrupted every 12 h to record an electrochemical impedance spectrum (galvanostatic mode: $i = 10 \text{ mA cm}^{-2}$, $\Delta i = 0.8 \text{ mA cm}^{-2}$, $10^5 \text{ Hz} > f > 0.15 \text{ Hz}$) and a cyclic voltammogram (scan rate = 5 mV s^{-1} , from 0 to 1 V vs. Hg–HgO/1 M KOH).

The data points of the lifetime measurements, Fig. 2, were acquired in the middle of a 12 h cycle, e.g. 6 h after the beginning of the polarization. A total of six experiments were carried out and progressively stopped at different times (250, 500, 750, 1000, 1800 and 3000 h). Statistic data² were obtained from all tests except for

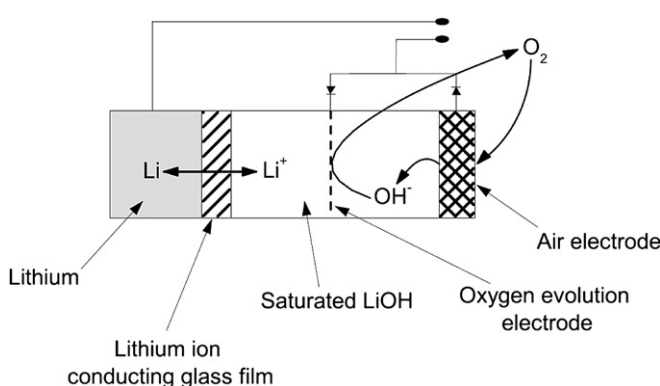


Fig. 1. Schematic diagram of the aqueous Li-air cell developed at EDF. It contains 3 electrodes: one Li negative electrode and a dual positive electrode composed of a thin oxygen evolution electrode (in the liquid aqueous solution) and an air electrode for oxygen reduction.

¹ 3000 h is the equivalent to about 150,000 km of operation for a combustion engine.

² There are six replicates up to 250 h, five replicates up to 500 h, four replicates up to 750 h, three replicates up to 1000 h and 2 replicates up to 1800 h.

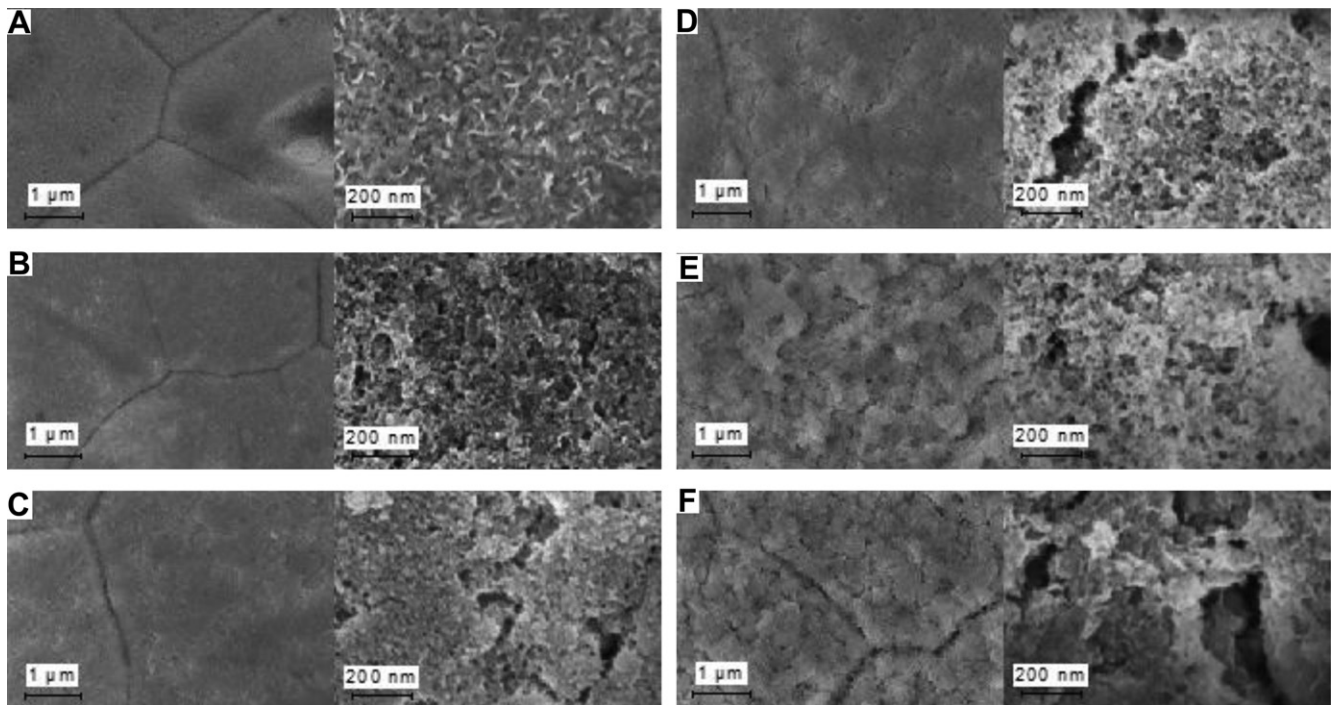


Fig. 3. SEM observations of the 316L stainless steel surface after 250 (A), 500 (B), 750 (C), 1000 (D), 1800 (E) and 3000 (F) hours of operation.

the 3000 h run, which has only been performed once. Statistical information (error bars) is therefore only given for durations below 1800 h. All electrochemical tests were performed in pure 5 M LiOH electrolyte in order to be more representative of the final electrolyte of the batteries (the Li-air battery will mostly operate beyond the saturation threshold of LiOH [9]). After each electrochemical experiment, the electrodes were delicately rinsed with demineralized water in order to remove traces of LiOH and prevent surface carbonation.

SEM observations were carried out with a HIROX SH-1500 SEM equipped with an XFLASH 410-H semiconductor Silicon Drift Detector, controlled with Esprit® V1.8 software; coupled elemental analyses were performed by X-EDS, at an accelerating voltage of the SEM of 10 kV. This low value was chosen as a compromise to limit the electron beam penetration depth to the surface layers [27], whilst keeping enough energy to collect information on the Cr, Fe and Ni elemental compositions. The X-EDS spectra were averaged on 10 different measurement locations in different areas of the samples. TEM observations were carried out using a Tecnai G2 20 F microscope operating at 200 kV.

The corrosion products of the working electrode were quantitatively analyzed by determining the amount of iron, chromium and nickel electrodeposited on the counter electrode.³ Each counter electrode was dissolved in a minimum of *aqua regia* and then demineralized water was added to 50 mL. The elemental analysis data were acquired with an ICP-AES Thermo ICAP 6500. The determination of the residual corrosion products in the electrolyte was not possible because of the high LiOH concentration: the required dilution would have led to a maximum resolution limit of 0.7 mg, too low to provide any additional information.

XPS measurements were performed at 10^{-10} mbar with a XR3E2 apparatus (Vacuum Generator) using a Mg Ka X-ray source (1253.6 eV) and a hemispherical analyzer at constant pass energy of 30.0 eV. Before the measurement, each sample was degassed for approximately 20 h in the vacuum chamber. The C_{1s} line at 284.6 eV was used as the reference binding energy (BE) for all core levels [28]. The analyses were carried out at an angle of 90° between the sample surface and the analyzer. Relative elemental concentrations were determined using Scofield cross-sections [29] corrected for the kinetic energy of the particular photoelectrons.

X-ray diffraction patterns were recorded with a PANalytical X'Pert Pro MPD (Bragg–Brentano configuration) operating at 45 kV and 40 mA using CuK α radiation. The 2θ angle was varied from 8° to 85° using a step size of 0.04° accumulating data for 14 s per step with sample rotation. The X-ray beam incidence angle was set at 0.75° (grazing incidence, GIXRD).

Raman spectra were acquired using a Raman microscope (Renishaw®) with an Ar⁺ laser operating at 540 nm.

The SEM, TEM, XRD and Raman analyses were performed on electrodes after a relaxation time superior to one week. Only for the XPS analyses, was the electrode polarized immediately prior to the measurements.

3. Results

3.1. Global results

The results obtained during the 3000 h of OER operation are given in Fig. 2. The small error bars demonstrate the reproducibility of the physicochemical phenomena in these conditions.

The variations of current density monitored around 1000 h of operation can be attributed to a change in concentration of the electrolyte (both the OER and the hydrogen evolution reaction, at the counter-electrode, consume water) and to its replacement. At 1800 h of operation, the electrolyte and the counter-electrode had to be replaced, the latter because the electrical connection had

³ Since the counter-electrode operates as a cathode (the working electrode being the OER anode) at a potential always below -1 V vs. Hg/HgO – 1 M KOH during operation, the migration and redeposition of the cations of these elements are favored.

become defective. Also, in contrast to the beginning of the test, the copper counter electrode had dissolved and formed of a black deposit on the working electrode, which reduced the performances, as shown in Fig. 2. It is possible that the partial dissolution of the working electrode (cf. Section 3.3.1) was too limited to stabilize the counter-electrode by the cathodic electrodeposition of corrosion products (especially Fe). After 2200 h, the working electrode was cleaned mechanically with a wet paper to remove the black copper (inactive) deposit that inhibited the 316L working electrode operation. The electrolyte was also changed and the copper counter-electrode was replaced by a 316L electrode, in order to finish the test. These operations resulted in an improvement of the performance. With the exception of these experimental problems, the performances of the electrode were stable throughout the whole test. The next section will focus on the performances obtained up to 1800 h of operation, which shows sufficient reproducibility.

Overall, the working electrode behavior exhibits two trends: an ascendant phase up to 250 h and then a stable period of performance. Furthermore, the SEM observations of Fig. 3 show the formation of a thin porous layer (grain boundaries remain visible on all observations). This layer is probably responsible for the good OER performance of the electrode after 250 h of operation, as will be discussed later. The presence of the thin porous layer (film) after 3000 h of operation demonstrates its good adherence, since the electrode was washed after 2200 h of operation. Tests carried out for a 316L electrode in 5 M KOH (not shown for brevity, see Ref. [26] for details) are similar, revealing that the observed behavior is not specific to LiOH electrolytes.

In order to understand the physico-chemical processes which occur during the aging test, some coupled *ex situ* analyses were performed on a 316L electrode which operated 250 h. This duration corresponds to the end of the activation period, *e.g.* the moment after which the performance of the electrode reaches its maximal (and stable) intensity.

3.2. Characterization of the layer formed after 250 h of operation

3.2.1. Cationic composition of the layer

The X-EDS analyses of Fig. 4 provide global information about the chemical modification of the electrode. Firstly, the presence of

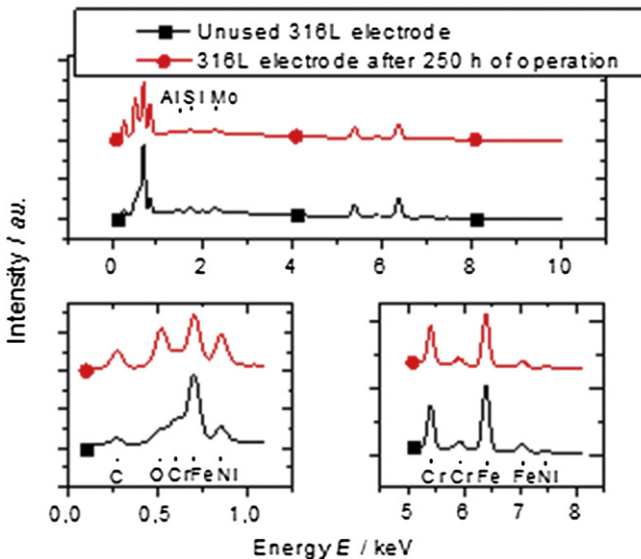


Fig. 4. X-EDS spectrum measured at the 316L stainless steel electrode surface before and after 250 h of operation (5 M LiOH; 0.8 V vs. Hg/HgO – 1 M KOH).

a small amount of pollutant is detected. The Al peak can be attributed to measurement artifacts: electrons of the incident beam that are backscattered by heavy elements of the sample (*e.g.* Fe, Ni or Cr) can reach the aluminum sample holder, as previously reported in Ref. [30]. The Si peak, of equal intensity on both new and used samples, is associated to the slight presence of Si in 316L (around 0.75% [31]), as is for Mo. Finally, the slight increase of C at the surface of the aged electrode probably results from some carbonation in the aging test (the solubility of CO_3^{2-} is low in LiOH [32]) or from contamination in contact with air, when the electrode was removed from the cell and rinsed prior its drying for the SEM and X-EDS analyses.

By analyzing the $\text{K}\alpha$ rays, one calculates a decrease in the Fe and Cr contained in the sampled volume, by 20% and 15%, respectively (Table 1). In opposition, the Ni content increases by 90%. The same values can be calculated with $\text{L}\alpha$ rays for Fe and Ni; evaluating the Cr content with the $\text{L}\alpha$ ray does not lead to an accurate value, because the Cr and O peaks are convoluted.

As the film formed has a low thickness (70 nm, *cf.* Fig. 8) and the electron beam energy is 10 keV, a 500 nm of penetration depth is estimated for compact steel [33]. The analysis therefore corresponds to a biphasic volume that includes the whole film plus an important part of the unmodified (bulk) 316L stainless steel. In order to get more precise information about the cationic concentration in the layer under study, two hypotheses can be put forth: (i) the film composition is homogenous in volume and (ii) the underlying bulk has the composition of 316L stainless steel. With these assumptions, an estimation of the Fe and Ni content in the film is possible, provided the Cr content is fixed (Fig. 5). Cr content was considered inferior to 10 at%, because of the low stability of Cr in our experimental conditions (alkalinity and potential) and superior to 5 at%, because lower values lead to unrealistic Fe contents below 0 at%. This representation highlights that the film is highly enriched in Ni (>60 at%).

Such surface enrichment in Ni, was confirmed by XPS spectra (Fig. 6) acquired by focusing on the major components present at the electrode surface, *i.e.* Ni, Fe, Cr and O. The cationic composition of the film is 83 at% of Ni, 10 at% of Fe and 7 a% of Cr (Table 2). Although, one has to be aware that the Cr content detected is close to the resolution limit of the XPS analysis (1% of the global composition [34]), these results agree with the X-EDS analyses of Fig. 5, which validate the cationic composition of the film.

The last important point highlighted by these analyses is the volume/depth homogeneity of the film. Indeed, the analysis depth of XPS measurement is *ca.* 5 nm [28,35], while X-EDS provides information about the whole volume of the catalytic layer, *i.e.* 70 nm (*cf.* Fig. 8).

3.2.2. Structure of the layer and structure of its oxides

The large oxygen content monitored by XPS (Table 2), is compatible with the presence of metal oxides. Although nickel

Table 1

$\text{K}\alpha$ or $\text{L}\alpha$ peak intensities for the various elements sampled and their variation during the aging test, as measured from the X-EDS spectra of Fig. 3.

Element	$\text{L}\alpha$ peak intensity/a.u.			$\text{K}\alpha$ peak intensity/a.u.		
	New sample	Aged sample	Variation	New sample	Aged sample	Variation
Cr				172	144	-16%
Fe	535	434	-19%	278	223	-20%
Ni	146	278	+90%	8.5	16	+88%
Mo	48	37	-23%			
C				55	127	+130%
Al				15	16	+7%
Si				38	36	-5%

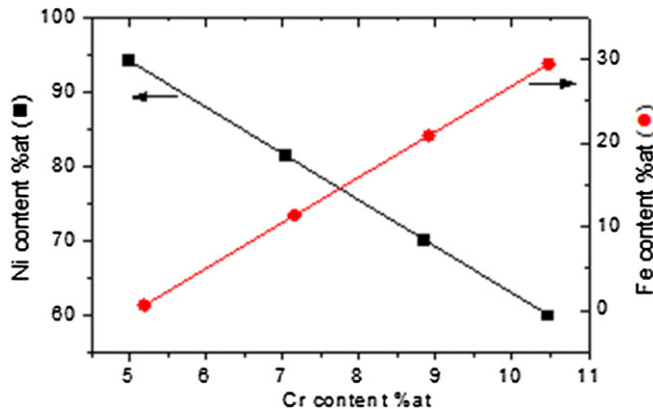


Fig. 5. Estimation of the Ni and Fe atomic content in the formed layer at the stainless steel surface after 250 h of operation (5 M LiOH; 0.8 V vs. Hg/HgO – 1 M KOH); calculations were performed by fixing the Cr content in the range 5–10 at%.

oxides are commonly well characterized by XRD [36–38]. Fig. 7 does not indicate any such oxides in the film, even though the experiments were performed in grazing incidence, e.g. were essentially sensitive to the extreme surface of the electrode. The most likely reason is the presence of an amorphous phase or of small crystallites ($\phi < 5$ nm). The TEM image of Fig. 8(B) and the electron diffraction pattern of Fig. 8(C) both validate such hypothesis.

The slice analysis of the electrode (Fig. 8(A)) reveals the structure of the thin catalytic layer. Its total thickness is *ca.* 70 nm, and is quite homogenous over the surface of the bulk electrode. One also observes a porous external layer of *ca.* 45 nm in thickness. These dimensions confirm the SEM observation of Fig. 3. In contrast, the intern part of the film, in contact with the bulk electrode, is more compact and is *ca.* 25 nm-thick.

3.2.3. Identification of the nickel oxide phase

Since the chemical phase(s) of the Ni-based compound(s) were not identified by XRD, the chemical bonds in the film were studied by Raman spectroscopy (Fig. 9). The Raman spectrum of the oxides film on 316L was compared to that of a film formed under the same electrochemical process, at the surface of a pure nickel electrode.⁴

The peaks measured have exactly the same position, which demonstrates the presence of similar major compounds at the surface of both electrodes. According to Refs. [39–43], these characteristic wavelengths ($\nu_1 = 460$ cm^{−1} and $\nu_2 = 525$ cm^{−1}) correspond to the Ni–OH and Ni–O vibrations mode in Ni(OH)₂. Despite the lack of agreement in the literature about specific wavelengths, if we refer to Deabate et al. [40], the compound likely is α -Ni(OH)₂, *e.g.* highly hydrated nickel hydroxides.

The analysis of the oxygen content in the film, evaluated by XPS (Fig. 6), confirms the presence an α -Ni(OH)₂ phase. The 2p_{3/2} peak position for nickel, iron and chromium are 855.5, 711 and 580.6 eV, respectively. Since these measurements were carried out immediately after polarization, the presence of a blend of Ni^{II} and Ni^{III}, Fe^{III} and Cr^{VI} (the characteristic peak for Cr^{III} is near 577 eV) is likely [44–48]. Therefore, in accordance with the thermodynamical data [49,50],⁵ the film contains Ni(OH)₂ or NiOOH, FeOOH and CrO₃. Hydroxide phases of Cr^{VI} were not indicated in the thermodynamical table, but as the Cr content is low (Table 2), that only slightly affects the results. In summary, each iron and nickel atom is linked to 2 oxygen atoms and each chromium atom is linked to 3

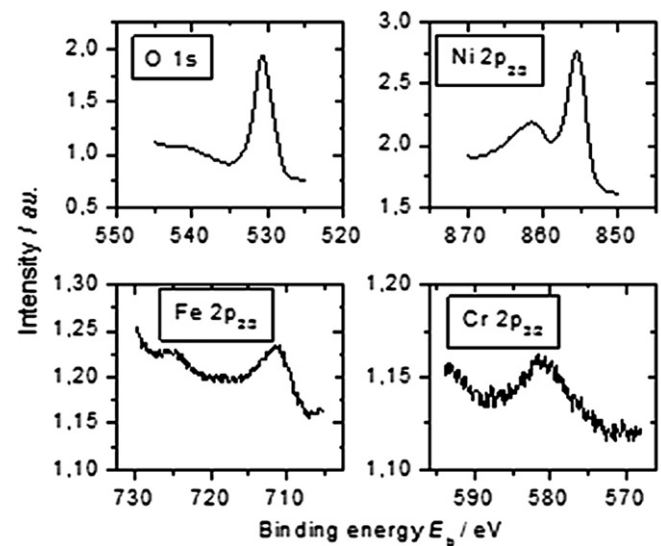


Fig. 6. High resolution XPS spectra measured at the 316L stainless steel surface after 250 h of operation (5 M LiOH; 0.8 V vs. Hg/HgO – 1 M KOH).

oxygen atoms. Knowing the global composition of the film (Table 2), one can calculate a ratio of 2.3 free oxygen atoms for each metallic cation, which validates the hypothesis of highly hydrated phases.

Hashimoto [51] found similar results for a study of nickel-based alloys under polarization at 0.2 V vs. SCE in 50 wt% NaOH, but he found a lower quantity of free water molecules for each metallic cation: 0.6. This difference is ascribed to the high electrode potential favoring α -Ni(OH)₂ formation [52–54]. In addition, the value of 2.3 free water molecules is possible, French et al. [55] having indicated that each α -Ni(OH)₂ moiety can contain up to 8 water molecules. More information about the electrochemical nickel hydroxide/oxohydroxide system can be found in Refs. [26,52,53,56–59].

3.2.4. Discussion

By using several analytical techniques, we demonstrated that the layer formed at the 316L stainless steel electrode during the aging test is largely composed of nanocrystalline nickel hydroxides. Its cationic composition, 83 at% of nickel, 10 at% of iron and 7 at% of chromium, is *a priori* consistent with the electrochemical measurements, since nickel oxides are known to have some electrocatalytic properties toward the OER.

Abreu et al. [60], in a similar study on a nickel-based alloy (Cr: 29%; Ni: 43%; Fe: 22%), monitored the formation of a surface film enriched in nickel hydroxides, during voltammetric sweep in 0.1 M NaOH (scan rate = 1 mV s^{−1}; $-1.4 < E < 0.6$ V vs. Hg/HgO – 0.1 M KOH). They also studied the behavior of three classical steels (AISI 430, AISI 304 and AISI 316) in the same conditions. Contrary to the nickel-based alloy, the steel surfaces were enriched in iron oxides. However, for austenitic steels (AISI 304 and AISI 316), an enrichment of Ni⁰ was also monitored at the oxide/metal interface.

Table 2

Film composition formed at the surface of the working electrode derived from the XPS measurements of Fig. 5.

Element	Position (eV)	Sensibility factor	Intensity a.u.	Atomic composition of the layer	Cationic composition
O	530.7	2.51	305	82 at%	
Ni	855.5	13.04	220	15 at%	83 at%
Fe	711	9.68	23	2 at%	10 at%
Cr	580.6	6.9	14	1 at%	7 at%

⁴ The reader can refer to Ref. [25] for a complete description of the electrochemical behavior of the nickel electrode in our test condition.

⁵ Only hydroxide phases were considered because of the present test conditions.

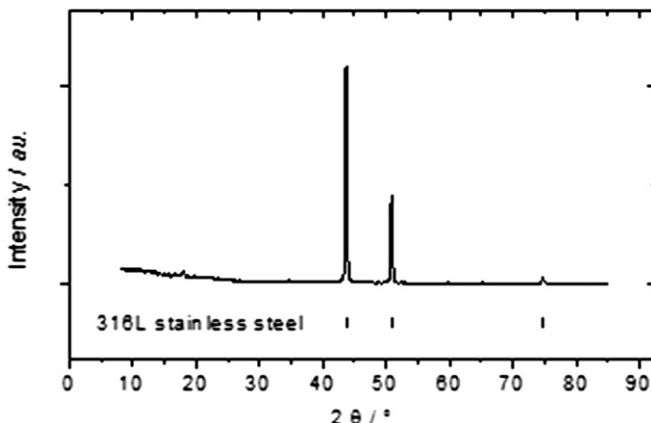


Fig. 7. GIXRD pattern of the 316L stainless steel surface after 250 h of operation (5 M LiOH; 0.8 V vs. Hg/HgO – 1 M KOH).

These observations are compatible with our results. Indeed, in Ref. [60], steel electrodes were cycled in cathodic potential, until the potential of hydrogen evolution, *i. e.* –1.2 V vs. Hg/HgO – 0.1 M KOH. The reduction current, clearly visible on the voltammograms, signs nickel surface oxides reduction as well as the deposition of chromium and iron species, which had been dissolved in the previous anodic sequence. This explains why Ni^0 enrichment is located at the oxides/metal interface. In contrast, for the nickel-based alloys, the low concentration of iron and chromium is not sufficient to form a Ni free film covering the whole electrode surface after the redeposition process. In addition, this low concentration of iron and chromium on the external part of the electrode cannot reduce the nickel oxides (nickel being electrochemically more stable than iron and chromium [49,60]).

On the contrary, during our test conditions, the 316L electrode was only subjected to potentials superior to 0 vs. Hg/HgO – 1 M KOH, incompatible with any electrodeposition process of the dissolved

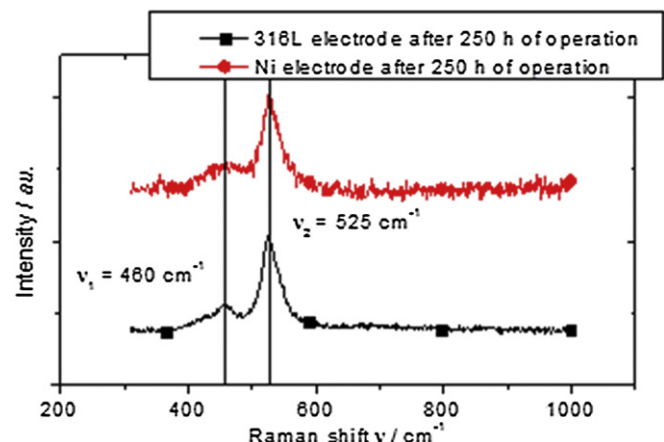


Fig. 9. Raman spectra measured at the 316L stainless steel surface or the surface of a pure Ni electrode after 250 h of operation (5 M LiOH; 0.8 V vs. Hg/HgO – 1 M KOH).

iron/chromium species. Moreover, the high alkalinity of the electrolyte stabilizes nickel oxides compared with iron and chromium oxides [49,61–63].

3.3. Behavior in operation

The physicochemical data of the previous sections clarify the mechanism of the catalytic layer formation and the origin of its catalytic properties. The voltammograms acquired between each constant polarization period further provide *in situ* information.

3.3.1. Film growth mechanism

Fig. 10 displays the first cyclic voltammograms obtained between each 12 h polarization period. The evolution of the oxidation peak, observed at 0.45 V vs. Hg/HgO/1 M KOH, is of great interest to understand the film formation mechanism. As discussed

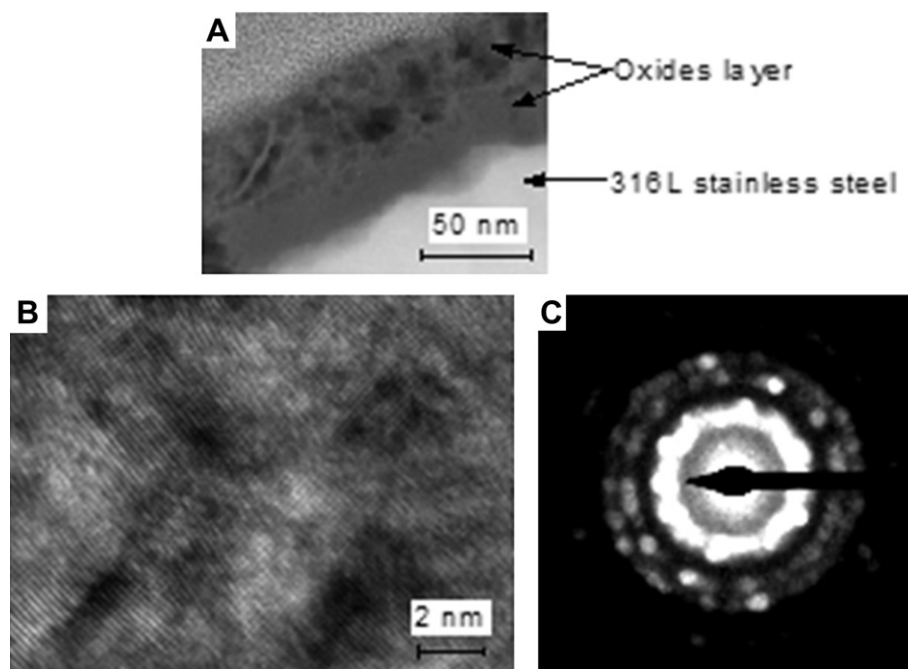


Fig. 8. TEM observation (A and B) of the oxides layer formed at the 316L stainless steel surface after 250 h of operation (5 M LiOH; 0.8 V vs. Hg/HgO – 1 M KOH); electron diffraction pattern of the oxides layer (C).

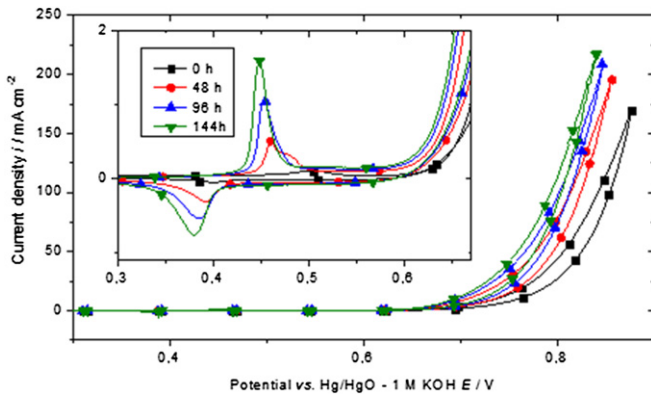


Fig. 10. Evolution of cyclic voltammograms measured on the 316L stainless steel during the first 144 h of operation (5 M LiOH; scan rate = 5 mV s⁻¹; T = 25 °C).

in Section 3.2, this peak can be attributed to the $\text{Ni(OH)}_2/\text{NiOOH}$ transition [47,51]. In that respect, NiOOH is likely to be the OER catalytic species at the surface of the electrode [53]. The observed negative shift of the peak is indeed a well-known behavior of nickel oxides in alkaline medium, linked to the progressive apparition of a more important fraction of $\gamma\text{-NiOOH}/\alpha\text{-Ni(OH)}_2$ in the layer [53,54,59]. This agrees with the previous analyses: at the beginning of the experiment, the layer was thin enough to enable its complete dehydration during the cathodic sweep, but the layer growth prevented its complete dehydration, and alternatively favored the increase of $\gamma\text{-NiOOH}/\alpha\text{-Ni(OH)}_2$ instead of $\beta\text{-NiOOH}/\beta\text{-Ni(OH)}_2$. Although Fe and Cr also have electrochemical contribution in this transition area (see the following sections), as a first approximation, the total electrochemical capacity can be attributed to the $(\text{Ni}^{\text{III}}/\text{Ni}^{\text{II}})$ couple only for the sake of simplicity.

Fig. 10 also shows a rise in intensity of the electrochemical peaks. This intensity being relative to the quantity of Ni^{II} or Ni^{III} contained in the catalytic layer [53,64], this evolution provides precise information about the growth of the layer. The surface charge involved in the $(\text{Ni}^{\text{II}}/\text{Ni}^{\text{III}})$ reaction continuously grows during the activation period (250 h of operation, Fig. 11). Since a thickness of 70 nm was measured by TEM (Fig. 8), a growth by electromigration, such as proposed by Medway and et al. [64] for a film growth at the surface of a nickel electrode during electrochemical cycling, is improbable. Medway and et al. indeed indicated that the layer growth by electromigration stops after 50 h of cycling, which corresponds to a thickness of 8 nm. It is important to note that this result is not linked to the use of the 316L stainless

steel electrode, a similar behavior has been observed for a pure nickel electrode [26]. Therefore, the film growth mechanism is most likely to be an anodic dissolution/precipitation process. During the electrode polarization, the metal species (at an oxidation state 0) are dissolved through the formation of ions which instantly precipitate at the electrode surface because of their low solubility. By comparing the solubilities of Ni, Fe and Cr ions, the dissolution–precipitation process provides a good explanation for the high Ni oxides content in the catalytic layer. Moreover, such a mechanism also accounts for a thick layer growth, in contrast to the electromigration mechanism, and is also compatible with the long-term stability monitored (3000 h of stable operation). Although the dissolution–precipitation mechanism leads to the formation of a porous layer, the part of the bulk electrode not coated with oxides is protected from dissolution by the formation of bubbles, which remain trapped in the porosity of the film and prevent the electrolyte access to the bare stainless steel. When the polarization is stopped, the bubbles are released and electrolyte can again access to the bulk electrode, which enables the growth of the layer at the start of the next polarization period (Fig. 12). In addition, this behavior explains why the growth slows down for long operation times (Fig. 13): thick layers hinder the electrolyte access to the bulk electrode.

In addition to the 316L stainless steel electrode behavior, this study highlights the critical phase which impacts the system stability: the anodic potential applied produces a very moderate corrosion of the electrode and a slight 316L stainless steel consumption (the charge passed for O_2 evolution during the 3000 h test is ca. 10^5 times larger than for 316L corrosion, as will be described below).

3.3.2. Evaluation of the long term stability of the electrode

The 316L stainless steel electrode displays stable catalytic performances over 3000 h of operation (Fig. 2), but one can wonder whether this stability of catalytic performance reflects the physical stability of the 316L electrode. By considering the measured surface charges involved in the $(\text{Ni}^{\text{III}}/\text{Ni}^{\text{II}})$ transition, the chemical composition and the growth mechanism of the film, the consumption of the electrode can be estimated. The model used for the calculation takes account of three formulated hypotheses: (i) the chemical composition is constant after the end of the activation period, e.g. 250 h; (ii) all nickel species precipitate at the electrode surface; (iii) the surface charge involved in the $(\text{Ni}^{\text{III}}/\text{Ni}^{\text{II}})$ transition contains the contribution of the Fe and Cr species in the catalytic layer. With these assumptions, the surface charges measured can be calculated: they correspond to 11.3% of the total dissolved species; the dissolved corrosion products are composed of 80% of iron species and 20% of chromium species.

Fig. 13 displays the surface charge involved in the $(\text{Ni}^{\text{III}}/\text{Ni}^{\text{II}})$ transition and the corresponding calculated bulk electrode consumption needed to form the film: the electrode consumption is only 315 nm after 1800 h of operation.⁶ This low value highlights the very low impact of the 316L electrode corrosion in operation, which clearly demonstrates that 316L electrodes can be used as specific OER electrodes in the aqueous lithium–air systems. Furthermore, this result demonstrates that a thin (lightweight) electrode can be used for a long period: this third electrode would not penalize energy density of the overall system.

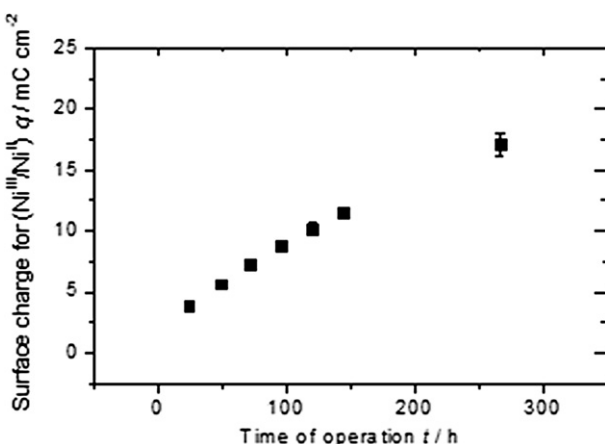


Fig. 11. Evolution of the surface charge for $(\text{Ni}^{\text{III}}/\text{Ni}^{\text{II}})$ peak recorded on the cyclic voltammograms during the electrode activation period (5 M LiOH; T = 25 °C).

⁶ The total coulometry for the 3000 h of test would correspond to a consumption of the 316L by 5 cm (3e⁻ per corroding Fe atom) to 7 cm (2e⁻ per corroding Fe atom) of metal if no O_2 was generated; this is 5 orders of magnitude away from the measured corrosion of the 316L electrode, therefore demonstrating the OER is nearly exclusive of corrosion reactions.

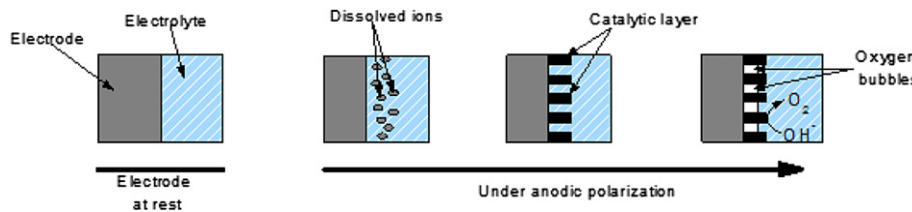


Fig. 12. Scheme of the catalytic film formation during the polarization period.

In order to validate the estimation of the bulk electrode consumption, we compared these calculations with an experimental measurement of the corrosion products. Since it was not possible to detect the presence of nickel and chromium species up after 1800 h of operation, we focused the comparison on iron. The quantity of dissolved iron, measured by ICP-AES, was plotted against the estimation of dissolved iron given by the model (Fig. 14). The correlation between the model and the experiment is good: the slope and the regression coefficient are close to 1. The negative constant of 64 μg implies a loss of matter which does not evolve with time, most likely due to the cleaning of the counter electrode prior the chemical analyses.

3.4. Electrocatalytic performance

3.4.1. Origin

Fig. 15 shows the voltammetric profiles (from Fig. 10) versus the surface charge of the $(\text{Ni}^{\text{III}}/\text{Ni}^{\text{II}})$ transition. Since NiOOH is the active species of OER [53], this figure highlights the electrocatalytic properties of active sites during the activation period.

An important drop of the active site performance is observed between the beginning and the 48th hour of operation. The decrease of iron and chromium content presented in Section 3.2 is consistent with such rapid drop. Indeed, in the case of spinel-type catalysts, Singh et al. [65–68] have shown a beneficial effect of the interactions between low- d electrons structure (e.g. Cr, V) and high- d electrons structure (e.g. Fe, Ni, Co). It is a common phenomenon, defined in the literature as the *hypo–hyper d interbonding effect* which enables the reactivity and selectivity of catalysts to be modulated toward a specific reaction [35]. The *hypo–hyper d interbonding effect* is a short-distance phenomenon, because it involves interactions from the quantum properties of atoms: cations can only interact with their nearest neighbors [69]. That means that a perfect homogenization at atomic scale is needed to

observe this effect. It is therefore highly dependent on the fabrication procedure of the (electro)catalysts.

Experiments with pure nickel electrodes led to lower catalytic performance than the 316L electrode [26], even though the catalytic films have approximately the same cationic composition. This is probably due to the different insertion of Cr and Fe in the catalytic layers in the two cases. Whilst for the 316L stainless steel electrode, Fe and Cr atoms are integrated into the surface layer during the nickel species precipitation, which enables a perfect homogenization, the presence of Fe and Cr species in the film at the nickel electrode can only originate from anodic deposition of corrosion products of the stainless steel counter-electrode; they are dispersed in the film in an agglomerate form, incompatible with the *hypo–hyper d interbonding effect* mentioned above. Similarly, one cannot exclude that the initial additives (Mo, Mn, Si, etc.) in the 316L stainless steel also positively affect the catalytic performance.

Fig. 15 also shows the stabilization of the voltammograms obtained at 96 and 144 h whereas, in the same period, the global performance of the electrode keeps improving (Figs. 2 and 10). The former result indicates that the catalytic layer has reached its final cationic composition after 96 h (see Section 3.2), e.g. the one which is stable in our test conditions. If this is the case, the performance increase monitored after 96 h reflects an increase of the electrode roughness, a purely geometrical factor. Nevertheless, the layer keeps on growing all along the experiment (Fig. 13), whilst the measured current density stabilizes after 250 h of operation. That implies that the active sites, within the depth of the film, are blocked by bubbles that prevent any access to hydroxyl ions.

Since an activation of 250 h period of this electrode would be too long to be economically viable in a practical system, an *ex situ* process was developed to accelerate the film formation: 7 h are necessary, in comparison to 250 h, for having the best performance of the electrode (not shown here for brevity) [26].

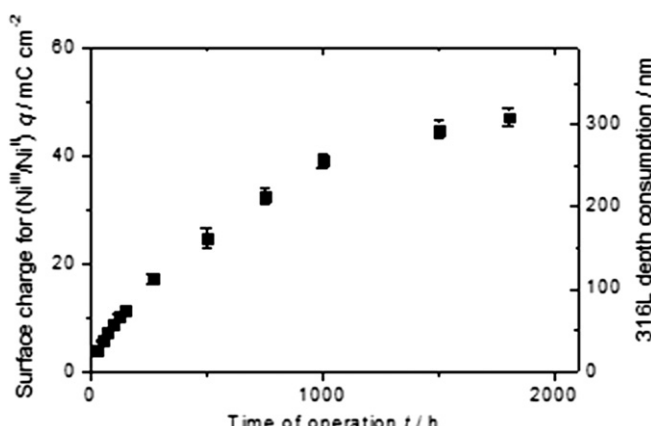


Fig. 13. Evolution of the total electrochemical surface charge for $(\text{Ni}^{\text{III}}/\text{Ni}^{\text{II}})$ peak and evolution of the 316L stainless steel electrode consumption during the aging experiment (5 M LiOH; $T = 25^{\circ}\text{C}$).

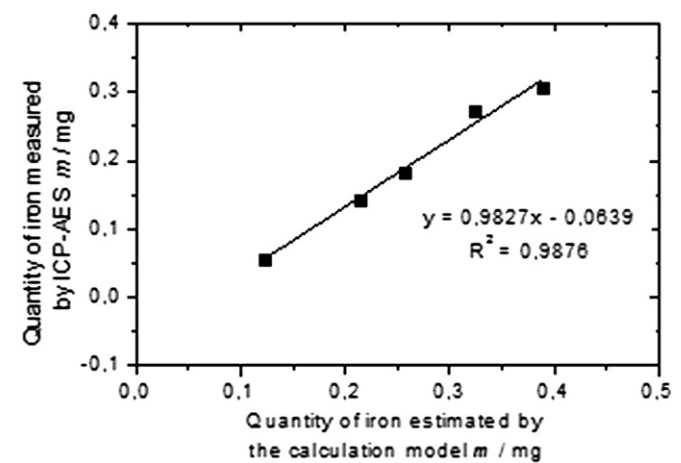


Fig. 14. Comparison of the quantity of dissolved iron measured by ICP-AES and estimated by the calculation model, for acquisitions at 250, 500, 750, 1000 and 1800 h of operation.

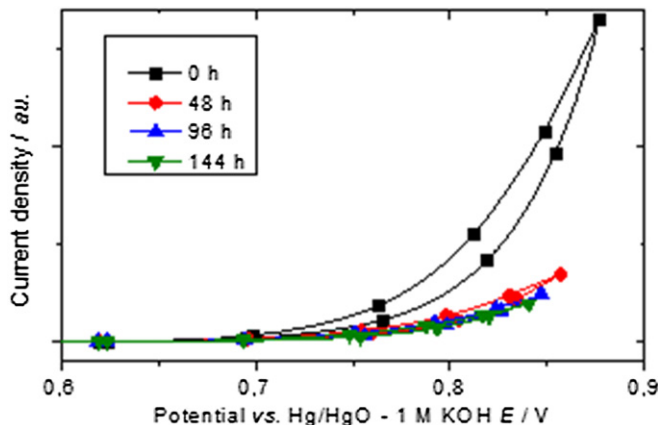


Fig. 15. Voltammetric profiles related to the real surface of the 316L electrode (5 M LiOH; scan rate = 5 mV s⁻¹; T = 25 °C).

3.4.2. Electrocatalytic performance of the 316L stainless steel electrode toward OER

In order to estimate the electrocatalytic performance of the surface layer (after 250 h of operation), a steady state polarization curve was measured at a potential sweep rate of 0.1 mV s⁻¹ in 1 M KOH (Fig. 16). The potential value measured at $i = 100 \text{ mA cm}^{-2}$, was compared to the ones obtained for various catalysts studied in the literature (Table 3). With a potential of 630 mV vs. Hg/HgO – 1 M KOH, the catalytic layer formed at the surface of the 316L stainless steel electrode is a very competitive catalyst. Only one catalyst shows a higher performance, but the study of Singh et al. [70] does not provide information about the electrode stability.

In addition, our catalytic layer was formed in a 5 M LiOH electrolyte. *De facto*, this result does not reflect the electrocatalytic performance of a film formed in another electrolyte (e.g. 1 M KOH or 5 M KOH). The equilibrium state of the film would probably differ in terms of cationic composition or roughness factor because of different constraints (electrolyte, applied potential, ...) [26]. It is therefore important to develop catalytic films in conditions close to those found in the application, e.g. in saturated LiOH for aqueous Li-air batteries.

From Fig. 16, a Tafel slope close to 40 mV dec⁻¹ is determined; a similar result was obtained by Lyons et al. [53] for nickel oxides used as OER catalyst. Considering the results obtained in 5 M KOH

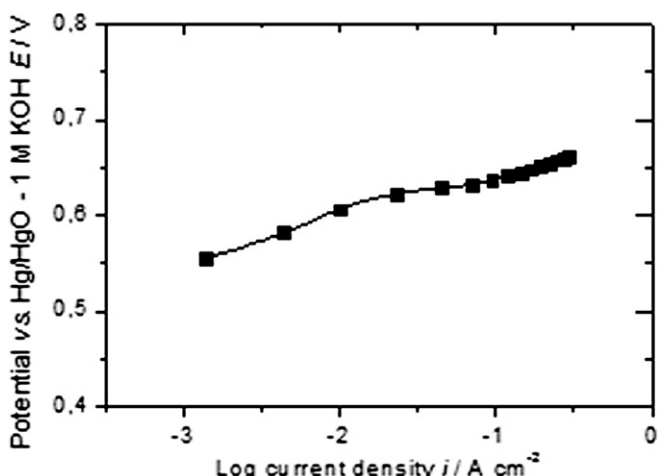
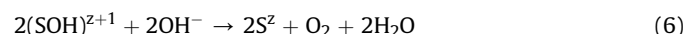


Fig. 16. OER steady state polarization curve for an aged 316L electrode (scan rate = 0.1 mV s⁻¹; 1 M KOH; T = 25 °C).

Table 3
Apparent electrocatalytic performance of some OER catalysts in 1 M KOH.

Catalyst	$E/\text{mV vs.}$ [Hg/HgO – 1 M KOH] at $i =$ 100 mA cm^{-2}	Ref.
Activated 316L stainless steel electrode	630	Fig. 16
La doped Co_3O_4 by microwaves	530	[69]
ZnCo_2O_4	600	[71]
Mixed oxides of Co and Ni	610	[72]
FeMoO_4	610	[66]
$\text{Cu}_{0.9}\text{Co}_{2.1}\text{O}_4$	623	[73]
$\text{CoFe}_{2-x}\text{Cr}_x\text{O}_4$	615–698	[74]
$\text{NiFe}_{2-x}\text{Cr}_x\text{O}_4$	650–690	[65]
$\text{NiFe}_{2-x}\text{V}_x\text{O}_4$	690	[64]
$\text{La}_{1-x}\text{Sr}_x\text{CoO}_3$	690	[75]
Co_3O_4 by thermal decomposition	700	[76]
Li doped Co_3O_4 by sol-gel process	760	[77]
$\text{LaNi}_{0.9}\text{Fe}_{0.1}\text{O}_3$	900	[78]

[26], it is possible to correlate these data to the reaction pathway proposed by Yeager (Equations (4)–(6)) [53], in which S correspond to the active sites of the reaction:



The difference between the performances measured in 5 M LiOH and in 1 M KOH is important. As shown in Fig. 10, the electrode potential is largely superior to 0.75 V vs. Hg/HgO – 1 M KOH at $i = 100 \text{ mA cm}^{-2}$ in 5 M LiOH. However, if only the electrolyte pH is taken into consideration [71], the change in electrolyte from 1 M KOH to 5 M LiOH would have decreased the potential by 0.030 V ($E_{\text{O}_2/\text{H}_2\text{O}}^0$ (5 M LiOH) ≈ 0.270 V vs. Hg/HgO – 1 M KOH; $E_{\text{O}_2/\text{H}_2\text{O}}^0$ (1 M KOH) ≈ 0.300 V vs. Hg/HgO – 1 M KOH). This observation highlights important catalytic problems when operating in LiOH and solutions to reduce the resultant additional overpotential will need to be addressed.

4. Conclusion

This study demonstrates the use of commercial 316L stainless steel as a stable OER electrode. This low-cost material shows stable performances over 3000 h of operation. The surface film responsible for these performances spontaneously and quickly forms by mild (surface) corrosion phenomena, which result from the system environment (highly oxidant medium, high alkalinity and anodic potential). It is composed of nanocrystalline oxides (83 at% of nickel oxides, 10 at% of iron oxides and 7 at% of chromium oxides) and is formed *via* an anodic dissolution–precipitation process. In addition, this electrode displays good physical stability, its consumption only amounts to 315 nm for 1800 h of operation.

Although corrosion can be a problematic phenomenon, its limited impact on this electrode makes it highly useful. Indeed, any deterioration of the film during operation will be spontaneously “healed” by its reformation, which overall stabilizes both the electrode and its electrocatalytic performance. This is a competitive advantage for the 316L electrode in contrast to common OER electrodes, which are composed of a thin catalytic layer deposited on a conducting substrate. In this latter case, a deterioration of the catalytic layer induces irreversible performance losses, because the catalytic film cannot be regenerated *in situ*. The second advantage

of such a corrosion process is that a cheap material matrix can be used in order to create *in situ* a film highly enriched in nickel (the most expensive element in the material) with high electrocatalytic activity toward OER.

Concerning the electrocatalytic performances, two phenomena make the 316L electrode highly competitive toward the OER. The first is a synergic effect (*hypo–hyper d interbonding effect*) due to the presence of well dispersed Fe and Cr in the catalytic film. The second is linked to the increase of the roughness of the electrode, which increases the electrochemical active surface area. Nevertheless, the negative influence of Li^+ ions also highlights an important problem of catalyst inhibition; this point has to be investigated further to improve the energetic efficiency of aqueous lithium–air systems.

This study shows that stable OER catalysts can be developed using alternative materials than those studied so far. Stainless steels, *via* their spontaneous adaptation to their environment are indeed prone to generate stable surface films with surprisingly high OER activity. Further development could be made by (i) looking for industrial processes to accelerate the formation of catalytic layer and (ii) investigating the behavior of others steels or alloys.

Acknowledgements

Financial support from Agence Nationale de la Recherche et de la Technologie (ANRT) is gratefully acknowledged. The authors would also like to thank Pr. B. Baroux for his useful explanation on the corrosion behavior of 316L as well as S. Coindeau, G. Berthomé, R. Michel, N. Sergent, C. Cossange and D. Loisnard for XRD, XPS, ICP, Raman spectroscopy, SEM and TEM experiment, respectively.

Appendix A. Supplementary data

Supplementary data related to this article can be found online at <http://dx.doi.org/10.1016/j.jpowsour.2012.11.133>.

References

- W.-j. Cui, H.-j. Liu, C.-x. Wang, Y.-y. Xia, *Electrochem. Commun.* 10 (2008) 1587–1589.
- Y. Iriyama, C. Yada, T. Abe, Z. Ogumi, K. Kikuchi, *Electrochem. Commun.* 8 (2006) 1287–1291.
- X.-Z. Liao, Z.-F. Ma, Q. Gong, Y.-S. He, L. Pei, L.-J. Zeng, *Electrochem. Commun.* 10 (2008) 691–694.
- H. Liu, G.X. Wang, D. Wexler, J.Z. Wang, H.K. Liu, *Electrochem. Commun.* 10 (2008) 165–169.
- P. Zhang, H.P. Zhang, G.C. Li, Z.H. Li, Y.P. Wu, *Electrochem. Commun.* 10 (2008) 1052–1055.
- J.M. Zheng, Z.R. Zhang, X.B. Wu, Z.X. Dong, Z. Zhu, Y. Yang, *J. Electrochem. Soc.* 155 (2008) A775–A782.
- M. Chatenet, in: Séminaire IDEES, Paris, 2010.
- A. De Guibert, in: Séminaire IDEES, Paris, 2010.
- P. Stevens, G. Toussaint, G. Caillon, P. Viaud, P. Vinatier, C. Cantau, O. Fichet, C. Sarrazin, M. Mallouki, *ECS Trans.* 28 (2010) 1–12.
- S.J. Visco, E. Nimon, L.C. De Jonghe, in: *Encyclopedia of Electrochemical Power Sources*, Elsevier, Amsterdam, 2009, pp. 376–383.
- K.M. Abraham, Z. Jiang, *J. Electrochem. Soc.* 143 (1996) 1–5.
- A. Débart, J. Bao, G. Armstrong, P.G. Bruce, *J. Power Sources* 174 (2007) 1177–1182.
- T. Ogasawara, A. Débart, M. Holzapfel, P. Novák, P.G. Bruce, *J. Am. Chem. Soc.* 128 (2006) 1390–1393.
- J. Read, *J. Electrochem. Soc.* 149 (2002) A1190–A1195.
- J. Read, K. Mutolo, M. Ervin, W. Behl, J. Wolfenstine, A. Driedger, D. Foster, *J. Electrochem. Soc.* 150 (2003) A1351–A1356.
- S.J. Visco, E. Nimon, B. Katz, *ECS Meeting Abstracts*, 602 (2006) 389.
- S.J. Visco, Y.S. Nimon, United States Patent US2004/0197641 A1, 2004.
- S.J. Visco, E. Nomon, B. Katz, L.C.D. Jongle, M.Y. Chu, in: The 12th International Meeting on Lithium Batteries, Nara, 2004.
- P. Knauth, *Solid State Ionics* 180 (2009) 911–916.
- J.S. Thokchom, B. Kumar, *J. Electrochem. Soc.* 154 (2007) A331–A336.
- S. Hasegawa, N. Imanishi, T. Zhang, J. Xie, A. Hirano, Y. Takeda, O. Yamamoto, *J. Power Sources* 189 (2009) 371–377.
- N. Imanishi, S. Hasegawa, T. Zhang, A. Hirano, Y. Takeda, O. Yamamoto, *J. Power Sources* 185 (2008) 1392–1397.
- K. Kinoshita, *Electrochemical Oxygen Technology*, John Wiley & Sons, Inc., New York, 1992.
- L. Jörissen, *J. Power Sources* 155 (2006) 23–32.
- G. Toussaint, P. Stevens, L. Akrou, R. Rouget, F. Fourgeot, *ECS Trans.* 28 (2010) 25–34.
- F. Moureaux, in Ph-D thesis, Institut Polytechnique de Grenoble, 2011.
- K. Kanaya, S. Okayama, *J. Phys. D. Appl. Phys.* 5 (1972) 43.
- Y. Dali, in Ph-D thesis, Ecole Nationale Supérieure des Mines de Saint-Etienne, Saint-Etienne, 2007.
- J.H. Scofield, *J. Electron Spectrosc. Relat. Phenom.* 8 (1976) 129–137.
- E. Guilmot, A. Corcella, M. Chatenet, F. Maillard, F. Charlot, G. Berthomé, C. Iojoiu, J.-Y. Sanchez, E. Rossinot, E. Claude, *J. Electrochem. Soc.* 154 (2007) B1106–B1114.
- In: AK Steel Corporation. http://www.aksteel.com/pdf/markets_products/stainless/austenitic/316_316L_Data_Sheet.pdf, 2007.
- D.R. Lide, *CRC Handbook of Chemistry and Physics*, New York, 2005.
- R. Reichelt, in: P.W. Hawkes, J.C.H. Spence (Eds.), *Science of Microscopy*, Springer, New York, 2007, pp. 133–272.
- H.J. Mathieu, E. Bergmann, R. Gras, *Analyse et technologie des surfaces: couches minces et tribologie*, Presses polytechniques et universitaires romandes, 2003.
- F. Micoud, in Ph-D thesis, Institut Polytechnique de Grenoble, Grenoble, 2009.
- F. Bardé, M.R. Palacín, B. Beaudoin, P.A. Christian, J.M. Tarascon, *J. Power Sources* 160 (2006) 733–743.
- W.-K. Hu, X.-P. Gao, D. Noréus, T. Burchardt, N.K. Nakstad, *J. Power Sources* 160 (2006) 704–710.
- X. Wang, H. Luo, P.V. Parkhutik, A.-C. Millan, E. Matveeva, *J. Power Sources* 115 (2003) 153–160.
- S.I. Cordoba-Torresi, C. Gabrielli, A.H.-L. Goff, R. Torresi, *J. Electrochem. Soc.* 138 (1991) 1548–1553.
- S. Deabate, F. Fourgeot, F. Henn, *J. Power Sources* 87 (2000) 125–136.
- C.A. Melendres, S. Xu, *J. Electrochem. Soc.* 131 (1984) 2239–2243.
- J. Nan, Y. Yang, Z. Lin, *Electrochim. Acta* 51 (2006) 4873–4879.
- I.J. Oblonsky, T.M. Devine, *Corros. Sci.* 37 (1995) 17–41.
- A.F. Carley, S.D. Jackson, J.N. O'Shea, M.W. Roberts, *Surf. Sci.* 440 (1999) L868–L874.
- L. Freire, M.J. Carmezim, M.G.S. Ferreira, M.F. Montemor, *Electrochim. Acta* 55 (2010) 6174–6181.
- A.P. Grosvenor, M.C. Biesinger, R.S.C. Smart, N.S. McIntyre, *Surf. Sci.* 600 (2006) 1771–1779.
- A. Kocjan, C. Donik, M. Jenko, *Corros. Sci.* 49 (2007) 2083–2098.
- M. Schulze, R. Reissner, M. Lorenz, U. Radke, W. Schnurnberger, *Electrochim. Acta* 44 (1999) 3969–3976.
- M. Pourbaix, *Atlas d'équilibres électrochimiques*, Gauthier-Villars, Paris, 1963.
- S. Riedel, M. Kaupp, *Coord. Chem. Rev.* 253 (2009) 606–624.
- K. Hashimoto, K. Asami, *Corros. Sci.* 19 (1979) 427–435.
- H. Bode, K. Dehmelt, J. Witte, *Electrochim. Acta* 11 (1966) 1079–1087.
- M.E.G. Lyons, M.P. Brandon, *J. Electroanal. Chem.* 641 (2010) 119–130.
- G.A. Snook, N.W. Duffy, A.G. Pandolfo, *J. Power Sources* 168 (2007) 513–521.
- H.M. French, M.J. Henderson, A.R. Hillman, E. Vieil, *Solid State Ionics* 150 (2002) 27–37.
- B. Ash, J. Kheti, K. Sanjay, T. Subbaiah, S. Anand, R.K. Paramguru, *Hydrometallurgy* 84 (2006) 250–255.
- A. Delahaye-Vidal, B. Beaudoin, N. Sac-Épée, K. Tekaia-Elhsissen, A. Audemer, M. Figlarz, *Solid State Ionics* 84 (1996) 239–248.
- M. Figlarz, J. Guenot, S. Le Bihan, C.R. Acad. Sci. Paris C270 (1970) 2131.
- M. Wehrens-Dijksma, P.H.L. Notten, *Electrochim. Acta* 51 (2006) 3609–3621.
- C.M. Abreu, M.J. Cristóbal, R. Losada, X.R. Nóvoa, G. Pena, M.C. Pérez, *Electrochim. Acta* 51 (2006) 2991–3000.
- B. Beverskog, I. Puigdomenech, *Corros. Sci.* 38 (1996) 2121–2135.
- B. Beverskog, I. Puigdomenech, *Corros. Sci.* 39 (1997) 43–57.
- B. Beverskog, I. Puigdomenech, *Corros. Sci.* 39 (1997) 969–980.
- S.L. Medway, C.A. Lucas, A. Kowal, R.J. Nichols, D. Johnson, *J. Electroanal. Chem.* 587 (2006) 172–181.
- A.S. Anindita, R.N. Singh, *Int. J. Hydrogen Energy* 35 (2010) 3243–3248.
- R.N. Singh, J.P. Singh, B. Lal, M.J.K. Thomas, S. Bera, *Electrochim. Acta* 51 (2006) 5515–5523.
- R.N. Singh, J.P. Singh, A. Singh, *Int. J. Hydrogen Energy* 33 (2008) 4260–4264.
- R.N. Singh, N.K. Singh, J.P. Singh, G. Balaji, N.S. Gajbhiye, *Int. J. Hydrogen Energy* 31 (2006) 701–707.
- M.M. Jaksic, *Solid State Ionics* 136–137 (2000) 733–746.
- R.N. Singh, D. Mishra, Anindita, A.S.K. Sinha, A. Singh, *Electrochim. Commun.* 9 (2007) 1369–1373.
- B.G. Pound, R.P. Singh, D.D. Macdonald, *J. Power Sources* 18 (1986) 1–31.
- G. Wu, N. Li, D.-R. Zhou, K. Mitsuo, B.-Q. Xu, *J. Solid State Chem.* 177 (2004) 3682.
- B. Marsan, N. Fradette, G. Beaudoin, *J. Electrochim. Soc.* 139 (1992) 1889.
- R.N. Singh, N.K. Singh, J.P. Singh, *Electrochim. Acta* 47 (2002) 3873.
- S.K. Tiwari, P. Chartier, R.N. Singh, *J. Electrochim. Soc.* 142 (1995) 148.
- S.P. Singh, S. Samuel, S.K. Tiwari, R.N. Singh, *Int. J. Hydrogen Energy* 21 (1996) 171.
- F. Svegl, B. Orel, I. Grabec-Svegl, V. Kaucic, *Electrochim. Acta* 45 (2000) 4359.
- R.N. Singh, S.K. Tiwari, P. Chartier, J.F. Koenig, *New Mat. Electrochem. Sys.* 2 (1999) 65.